

## Article

# High Temperature Oxidation Behavior of High Al-Si Alloyed Vermicular Graphite Cast Iron for Internal Combustion Engine's Hot-End Exhaust Components

Rifat Yilmaz <sup>1,2</sup> , Fatma Bayata <sup>3</sup>  and Nuri Solak <sup>1,\*</sup> 

<sup>1</sup> Department of Metallurgical and Materials Engineering, Istanbul Technical University, 34469 Istanbul, Turkey; yilmazrif@itu.edu.tr or ryilmaz5@ford.com.tr

<sup>2</sup> Sancaktepe R & D Center, Ford Otomotiv Sanayi A.S., 34885 Istanbul, Turkey

<sup>3</sup> Department of Mechanical Engineering, Istanbul Bilgi University, 34060 Istanbul, Turkey; fatma.bayata@bilgi.edu.tr

\* Correspondence: solaknu@itu.edu.tr

**Abstract:** This study investigated the influence of high silicon (4.2 wt%) and varying aluminum (3.5–4.8 wt%) content on the high temperature oxidation behavior and thermophysical properties of SiMoAl vermicular graphite cast iron for hot-end exhaust components. Isothermal oxidation tests at 800 °C and nonisothermal oxidation tests in a dry-air atmosphere were conducted on SiMo nodular iron, along with two SiMoAl vermicular graphite cast iron variants alloyed with 3.5 wt% Al and 4.8 wt% Al. The investigations revealed the formation of a thin duplex layer of oxide scale, consisting of an iron-rich external oxide layer and continuous aluminum oxide at the metal/oxide interface. Although aluminum oxide acted as a protective barrier by impeding the solid-state diffusion of oxygen, severe subsurface oxidation was observed due to the interconnected vermicular graphite covered by aluminum oxides after decarburization. Furthermore, based on nonisothermal oxidation experiments, the effective activation energy of oxidation was found to be significantly increased by the addition of aluminum, even though the oxidation activation energies of SiMoAl samples exhibited small changes in comparison to each other. Additionally, thermophysical analysis demonstrated a substantial decrease in the thermal conductivity and a slight increase in the thermal expansion with the addition of aluminum.

**Keywords:** SiMoAl vermicular graphite cast iron; high-temperature oxidation; activation energy of oxidation; thermal conductivity; thermal expansion



**Citation:** Yilmaz, R.; Bayata, F.; Solak, N. High Temperature Oxidation Behavior of High Al-Si Alloyed Vermicular Graphite Cast Iron for Internal Combustion Engine's Hot-End Exhaust Components. *Metals* **2024**, *14*, 574. <https://doi.org/10.3390/met14050574>

Academic Editor: Shusen Wu

Received: 4 April 2024

Revised: 30 April 2024

Accepted: 3 May 2024

Published: 13 May 2024



**Copyright:** © 2024 by the authors. Licensee MDPI, Basel, Switzerland. This article is an open access article distributed under the terms and conditions of the Creative Commons Attribution (CC BY) license (<https://creativecommons.org/licenses/by/4.0/>).

## 1. Introduction

Ferritic high-silicon and molybdenum (SiMo) nodular cast iron is one of the most widely used materials in exhaust manifolds and turbocharger housings due to its desirable thermomechanical properties and its resistance to high-temperature corrosion [1–5]. These parts are subjected to cyclic thermal loads during the engine's operating condition. When selecting materials in these applications, thermomechanical properties, thermophysical properties, and high-temperature oxidation behavior are taken into consideration. However, as a result of ongoing enhancements in combustion engine efficiency and stricter legal emission regulations, the exhaust gas temperature has been increasing and is approaching a range of 800 °C to 1000 °C [5,6]. This temperature level exceeds the maximum limit for the existing material SiMo nodular iron, calling for the investigation of viable alternatives such as SiMo nodular cast iron alloyed with aluminum, chromium, or nickel to enhance its high-temperature capabilities. SiMo nodular cast iron demonstrates robust mechanical properties up to 500 °C; however, in the temperature range of 500 °C to 750 °C, there is a notable transition from the dominance of elastic strain amplitude to plastic strain amplitude during fatigue cycles [3,5,6]. This phenomenon is also observed in austenitic Ni-Resist

(D5S) cast iron, which has slightly higher mechanical properties than SiMo nodular irons above 500 °C, and notably, D5S stands out with its fatigue resistance at temperatures of 700 °C and above [3,6,7]. Another alternative, SiMo1000, shows improved fatigue life over SiMo under different mechanical strain amplitudes in an oxidized environment [6,8]. Significantly, SiMo1000's fatigue life is more dependent on graphite morphology than on environmental effects [6]. However, D5S still exhibits higher fatigue resistance above 700 °C compared to SiMo cast iron variants. Additionally, ferritic SiMo cast irons exhibit lower creep rupture stresses for equivalent values of the Larson Miller parameter compared to austenitic cast irons such as Ni-Resist D5S [9,10]. Despite these challenges, SiMo cast iron variants remain a cost-effective alternative to the more expensive austenitic D5S cast iron, especially for applications within the automotive industry.

Building on the exploration of alternatives, the addition of silicon and molybdenum as ferrite stabilizers to SiMo ductile iron has been shown to be the most effective method for improving its performance at elevated temperatures. Molybdenum improves creep resistance and machinability while diminishing toughness as a consequence of carbide segregation at grain boundaries [11–13]. The high silicon content increases the temperature of the ferrite–austenite transformation, which determines the maximum useful regime for SiMo nodular iron. In addition, silicon enhances high temperature oxidation resistance by forming a silicon-rich oxide layer. The high-temperature oxidation behavior of SiMo nodular cast iron has been studied in dry air, wet air (air + 10% H<sub>2</sub>O), and exhaust gas environments at elevated temperatures (650 to 1050 °C) by many researchers [14–21]. These studies showed that when SiMo cast iron was exposed to high temperatures in the presence of air and exhaust gases (synthetic diesel and gasoline), it formed a multilayered oxide scale. The scale was composed of three layers: the external layer was hematite and magnetite that expanded outwards, the internal layer was magnetite (Fe<sub>3</sub>O<sub>4</sub>) and fayalite (Fe<sub>2</sub>SiO<sub>2</sub>) that grew into the subsurface, and there was a thin protective film of silica (SiO<sub>2</sub>) at the metal/oxide interface. This thin silica film could be reacted with Fe, O, or FeO to form fayalite (Fe<sub>2</sub>SiO<sub>2</sub>) [22–24]. It was also reported that the silica film was discontinuous throughout the interface but still slowed down the oxidation kinetics [25]. The formation of the silica film was much more favorable at 800 °C than at 700 °C [26]. However, Lekakh et al. [19,27] showed that the protective and continuous amorphous silica layer obtained in the SiMo cast iron was limited at 700 °C since the oxygen permeability of the amorphous silica layer increased above 750 °C and promoted a decarburization reaction near the interface. The high pressure of CO gas from decarburization caused deformation of the metal matrix, which led to delamination in the brittle silica oxide layer. In addition, silica film formation below 650 °C was reported in the literature.

There are two kinds of oxidation that take place in cast iron. One is metallic oxidation, commonly known as scaling, and the other is the oxidation of carbon, which is referred to as decarburization. The decarburization process can occur via carbon diffusing outward, by oxygen diffusing inward, or by both. Graphite morphology and distribution has a vital role in this process [28]. Lamellar or vermicular graphite in cast iron is mainly oxidized through direct contact with the gas phase. On the other hand, spheroidal graphite decarburization in cast iron mostly occurs through solid-state diffusion of carbon to the metal/oxide interface. After the oxidation of graphite, voids or pores are developed that lead to oxygen penetration inside the metal matrix, causing subsurface oxidation. Lin et al. [29] and Guo et al. [30] demonstrated that flake graphite and vermicular graphite cast irons had worse high-temperature oxidation resistance compared to nodular cast iron due to severe subsurface oxidation. Since graphite flakes were almost interconnected to each other, they served as the primary core and pathway for oxidation. Furthermore, Lekakh et al. [19,27] reported that metal matrix oxidation and decarburization interact with each other. Decarburization impacted the oxide morphology and oxidation rate, and at the same time, the presence of oxides could slow down the decarburization rate for SiMo ductile iron.

The high-temperature performance of SiMo nodular iron can be improved by alloying with chromium, aluminum, vanadium, or nickel, which is recognized for having ability to

enhance the oxidation resistance of steel [16,31–34]. Ekström et al. [16] studied the effect of 0.5 to 1 wt% Cr and 1 wt% Ni on the high-temperature oxidation of SiMo ductile iron in air and exhaust gases. Carbon (3.2%), silicon (4.2%), and molybdenum (0.8%) contents were kept constant. It was reported that the addition of Cr increased the oxidation resistance in air at 700 °C and 800 °C by forming Cr-oxide phases in addition to the silicon oxide at the metal/oxide interface. However, the Cr-oxide phase was not observed in the exhaust gas environment at the elevated temperature. On the other hand, it was reported that the addition of nickel broke down the silica film, which decreased the oxidation resistance. Lakekh et al. [27] demonstrated that the addition of 1 wt% Cr created a mostly pearlitic microstructure and Cr-carbides located at grain boundaries.

Aluminum is another element that improves the high-temperature oxidation resistance of cast irons by forming a thin and impervious aluminum oxide film. In addition to oxidation resistance, adding aluminum into cast iron also increases the ferrite-to-austenite phase transformation temperature [35–38]. Cvetnic et al. [35] studied the oxidation behavior of ductile iron alloys containing Mo (1.5 wt%) and different combinations of aluminum (2–3 wt%) and silicon (3.5–4.5 wt%) between 700 °C to 1100 °C. Maximum oxidation resistance was obtained by ductile iron samples alloyed with 4.5 wt% Si and 3.0 wt% Al. The scale consisted of an external layer of iron oxides and an internal layer of aluminum and silicon oxides. Lakekh et al. [27,39] studied the static oxidation behavior and transient thermo-mechanical behavior of SiMo ductile iron alloyed with 3 wt% Si and 1.8 wt% Al–3.0 wt% Al. It was reported that the alumina film decreased the decarburization rate five to seven times at 800 °C as comparing to SiMo cast iron. SiMo3Al exhibited stronger oxidation behavior than SiMo1.8Al; however, this alloy was not protected from fracture formation during rapid thermal cycling, and the degradation of graphite precipitate was negatively impacted by increased aluminum content. Similar to the results from Cvetnic et al. [35] and Mervat et al. [31], multilayer oxide scale was observed, and aluminum-rich oxide scale was formed at the metal/oxide interface. In addition, ferritic iron matrices with nodular, chunky graphite or vermicular graphite are reported in the literature.

The majority of published research on ferritic SiMoAl cast iron has predominantly focused on the isothermal oxidation phenomenon, and all studied microstructures are fully ferritic and  $\kappa$  carbide-free. The aim of the present work is to investigate the nonisothermal oxidation behavior of SiMoAl vermicular graphite cast iron and to understand the impact of aluminum alloying on the activation energy of oxidation. This investigation of nonisothermal oxidation is complemented by a concurrent study of isothermal oxidation processes, microstructural analyses, and the examination of thermophysical properties. By combining investigations into thermophysical properties and oxidation behavior, this study provides useful insights for enhancing the performance of cast irons, especially in applications related to hot-end exhaust components.

## 2. Materials and Methods

### 2.1. Material Preparation

The studied cast iron alloys were produced in a 100 kg medium-frequency induction furnace by melting pig iron, steel scrap, and ferroalloys. Upon reaching a temperature of 1450 °C, pieces of 99.5% pure aluminium were added to the melt. The temperature was readjusted to 1450 °C, and then the melt was transferred to the ladle for magnesium treatment. During this process, ferrosiliconmagnesium (FeSi5Mg) was used for spheroidizing. Subsequently, the melt underwent secondary inoculation with ferrosilicon (FeSi75) in the ladle. The molten iron, maintained at over 1400 °C, was then poured into green sand molds composed of 82 wt% silica sand, 7 wt% bentonite clay as the binder, 6 wt% water, and 5 wt% sea coal. The total time from tapping to pouring was approximately 3.5 min. Three different compositions were cast in total. The chemical compositions of cast parts were analyzed by optical emission spectrometer, as shown in Table 1.

**Table 1.** Chemical composition given in wt% (Fe bal.).

Alloy	C	Al	Si	Mn	Cr	Mo	Mg
SiMo	3.2	-	4.33	0.25	0.08	0.81	0.03
SiMo3Al	2.9	3.5	4.2	0.23	0.09	0.20	0.03
SiMo4Al	2.9	4.8	4.2	0.21	0.09	0.20	0.03

The EDS-equipped scanning electron microscope (SEM) from ThermoFisher Scientific Axia ChemiSEM (Waltham, MA, USA) and X-ray diffraction (XRD) system from Malvern Panalytical Aeris (Malvern, UK) were utilized to observe the impact of aluminum alloying on the microstructure and graphite morphology.

### 2.2. Isothermal Oxidation Test

An isothermal oxidation test in air was carried out in an 800 °C box furnace. In order to perform the oxidation test, cast components were machined into a specimen with the shape of a rectangle and the dimensions of 15 mm by 10 mm by 5 mm. After milling, these specimens were ground to a 1000-grit finish using silicon carbide (SiC) abrasive paper. Upon completion of the 96 h test, the specimens were prepared for SEM and EDS analysis. To investigate oxide structures and phases from the cross section, oxide surfaces were coated with epoxy resin and cured in a furnace at 120 °C for 15 min. Thus, oxide surfaces were protected against damage caused by cutting. Each sample was then sliced vertically from the epoxy surfaces and subsequently ground using SiC paper down to a finish of 1200 grit. SEM equipped with EDS was used to analyze the oxide morphology, perform quantitative elemental analysis, and measure the thickness of oxide layers on the prepared cross-section surfaces.

### 2.3. Nonisothermal Oxidation Test and Evaluation of Kinetic Parameters

In a dry-air environment, nonisothermal oxidation experiments (Netzsch Model STA 449 F3 Jupiter (Selb, Germany)) were carried out to investigate the kinetics of oxidation. Disc-shaped thermogravimetry (TG) samples with a diameter of 4 mm and a thickness of 1.5 mm were prepared. The approximate weight of the samples was 130 mg. Experiments were conducted with various heating rates between RT and 1100 °C (5 K/min, 10 K/min, and 20 K/min). The TG and DSC baselines were calibrated by subtracting the predetermined baselines performed under the same conditions.

The Kissinger method was used to evaluate kinetic parameters following several nonisothermal thermogravimetric analyses [40,41]. It is the commonly used method for calculating the activation energy of thermally induced processes. The method relies on a few nonisothermal tests conducted at various heating rates using thermal analysis tools (DSC, DTA). Using the exothermic peak temperature at each heating rate, kinetic parameters are then determined. The activation energy can be derived from a single variable using the Kissinger technique, which does not require a reaction mechanism. The Kissinger equation is

$$\ln\left(\frac{\beta}{T_{max}^2}\right) = \ln\left(\frac{AR}{E_a}\right) - \frac{E_a}{RT_{max}} \quad (1)$$

where  $A$  represents the Arrhenius frequency factor and  $T_{max}$  is the temperature of the DTG plot's peak maximum. The activation energy  $E_a$  can be calculated using the slope of the graph of  $\ln\left(\frac{\beta}{T_{max}^2}\right)$  against  $\frac{1}{T_{max}}$ .

### 2.4. Measurement of Thermophysical Properties

In this study, several thermal conductivity and thermal expansion measurements were conducted for SiMoAl and SiMo samples. The laser flash analysis (LFA) technique was employed to measure thermal diffusivity of the investigated samples. LFA is a nondestructive and highly accurate method for measuring thermal diffusivity and subsequently evaluating

thermal conductivity. A Netzsche LFA467 HT Hyperflash (Selb, Germany) was used for the thermal diffusivity characterization. In this experiment, the sample was heated for a short period of time with a laser pulse, and then the temperature response was measured. The laser pulse induced an instant temperature rise on the sample's surface, which was then analyzed using a very sensitive infrared detector. The thermal conductivity was determined using the following equation based on the thermal diffusivity, specific heat, and density:

$$\kappa = \alpha\rho C_p \quad (2)$$

where  $\alpha$  is the thermal diffusivity,  $C_p$  is the specific heat capacity,  $\rho$  is the density, and  $\kappa$  is the heat capacity.

A dilatometer was employed to investigate the thermal expansion behavior of the studied samples. The dilatometer is a flexible tool that is commonly used to measure dimensional changes in materials as a function of temperature. In this study, a push rod dilatometer (Netzsche DIL402 Expedis Classic (Selb, Germany)), in which a sample is positioned between two rods and the changes in its length are measured with a high accuracy, was used. The sample's temperature-dependent expansion or contraction reveals important information about its thermal expansion coefficients and phase-transition temperatures. The dilatometer measurements enabled a detailed analysis of the thermal expansion characteristics of the SiMoAl samples in comparison to the reference material. The observed trends were crucial in understanding the impact of alloying elements on the thermal properties of the studied materials.

### 3. Results and Discussion

#### 3.1. Microstructural Analysis of SiMo and SiMoAl Cast Irons

The scanning electron microscopy (SEM) images of SiMo, SiMo3Al, and SiMo4Al are shown in Figure 1a–e. It was clearly observed that all three microstructures contain a stable ferrite phase, graphite precipitates, and carbides in the matrix. Graphite precipitates, with a spheroidal shape, were dispersed into the iron matrix independently of each other in three dimensions. After alloying with aluminum, the nodular structure of graphite converted into a vermicular form and nodularity decreased, as seen in Figure 1c,d. Additionally, chunky clusters of graphite were generated and randomly scattered throughout the matrix. The graphite size of samples containing aluminum was relatively smaller than that of SiMo iron. Based on previous studies [31,42–45], the diminished nodularity could be the result of the nonuniform and uneven segregation of aluminum surrounding graphite nodules. This irregular segregation of aluminum led to nonuniform carbon diffusion and graphite formation.

Skeleton-shape Mo-rich eutectic carbides and Fe<sub>2</sub>MoC and Mo<sub>6</sub>C precipitates were observed in the microstructure of SiMo (Figure 1b). However, small granular Mo-rich precipitates (Mo<sub>6</sub>C and Fe<sub>2</sub>MoC) were only formed in aluminum-alloyed SiMo cast irons due to the low content of Mo. In addition to the Mo-rich precipitates, the  $\kappa$  carbide form of Fe<sub>3</sub>AlC was observed in the matrix (Figure 1e), while Fe<sub>3</sub>AlC precipitates were seen as lamellar and shaped like a pearlite structure in the SiMo3Al matrix, while coarse-grained  $\kappa$  carbides and lamellar  $\kappa$  precipitates were both found in the SiMo4Al matrix. Microstructural analysis conducted on samples showed that the addition of aluminum in the structure induced an increase in the abundance of pearlite and  $\kappa$  carbide, although ferrite predominated in the SiMo nodular cast iron.

XRD results were in good agreement with the SEM results as well. The XRD pattern is shown in Figure 2 for specimens of SiMo, SiMo3Al, and SiMo4Al.  $\kappa$  carbide was observed in the XRD pattern of SiMo3Al and SiMo4Al. However, Mo-rich eutectic carbide was not found due to its low concentration in the iron matrix. The XRD result also showed that increasing the aluminum content in the structure increased the amount of the  $\kappa$  phase.

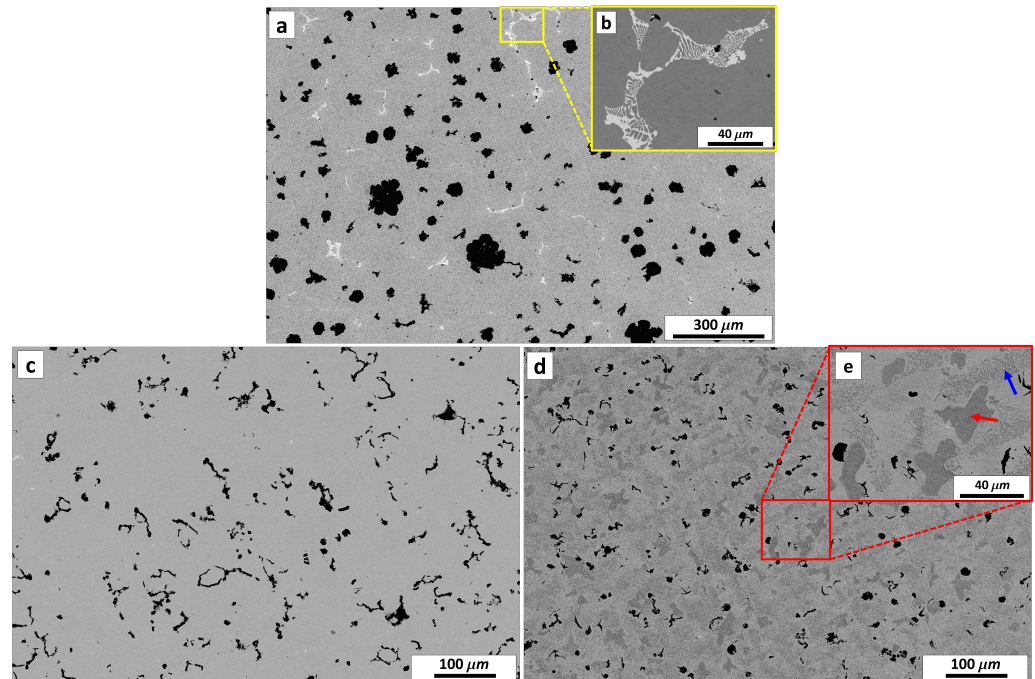


**Figure 1.** SEM images for SiMo, SiMo3Al, and SiMo4Al: (a) Microstructure of SiMo nodular iron. (b) Skeleton-shape Mo-rich eutectic carbides. (c) Microstructure of SiMo3Al vermicular iron. (d) Microstructure of SiMo4Al vermicular iron. (e) Lamellar  $\kappa$  carbides shown with blue arrow and coarse-grained  $\kappa$  carbides ( $\text{Fe}_3\text{AlC}$ ) shown with red arrow.

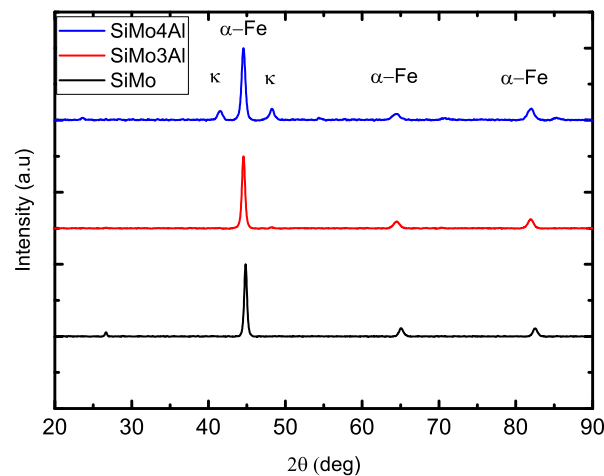


**Figure 2.** XRD phase analysis of SiMo, SiMo3Al, SiMo4Al.

### 3.2. Isothermal Oxidation Mechanism of SiMo and SiMoAl

While evaluating the impact of aluminum on the effective activation energy of oxidation and microstructure, understanding the oxidation mechanism of SiMoAl vermicular cast iron at elevated temperatures is crucial. Therefore, an isothermal oxidation test was conducted in air at a temperature of 800 °C, along with comparative studies using reference SiMo nodular iron.

First, the cross-sectional backscattered electron image of the oxide layer of SiMo nodular cast iron is presented in Figure 3 as a reference. The oxide layer was thick and porous. Porosity was mainly formed as a result of the decarburization of graphite nodules, which can lead to the growth of oxide quickly [16,29]. Oxygen can easily penetrate through these voids and cracks, resulting in the formation of a thick and nonprotective oxide layer.

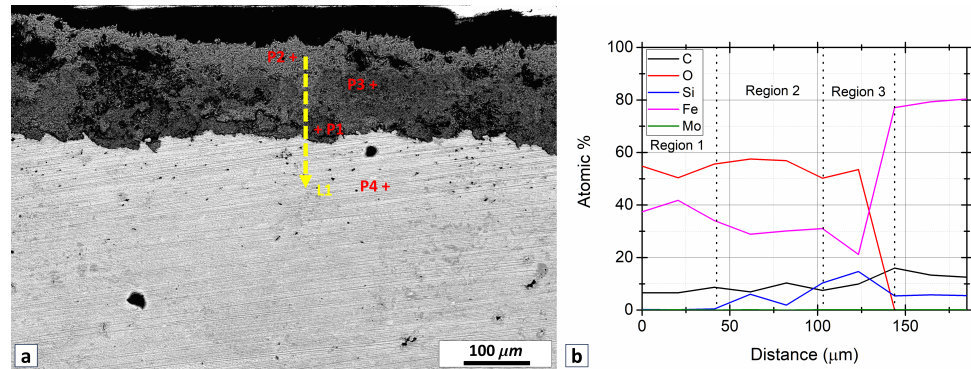


**Figure 3.** (a) Backscattered electron image of the oxide layer of SiMo nodular iron. Yellow line L1 shows the line scan direction, and P1, P2, P3, and P4 are the EDS points. (b) EDS line scan graph of L1.

SEM/EDS analysis of SiMo nodular iron showed that oxide film can be observed in three regions (Figures 3 and 4 and Table 2). The uppermost layer of the oxide film was called region 1/outer layer, and it was composed primarily of iron oxides. It was a type of oxide film that is continuous in nature. Iron silicon oxide-rich clusters were observed randomly distributed throughout the oxide in region 2, which was the inner section of the oxide. Region 3 was defined as the interface between the oxide and the metal matrix. In this region, as the iron content decreased, the silicon content increased, as shown in Figure 3b. The silicon concentration (14.7 at%) was higher than the content of this in region 2 (6.0 at%) and the matrix (5.5 at%). This result suggested that a thin layer of fayalite ( $\text{Fe}_2\text{SiO}_4$ ), silica ( $\text{SiO}_2$ ), or both could be seen, but the film thickness did not remain constant through the interface and was discontinuous.

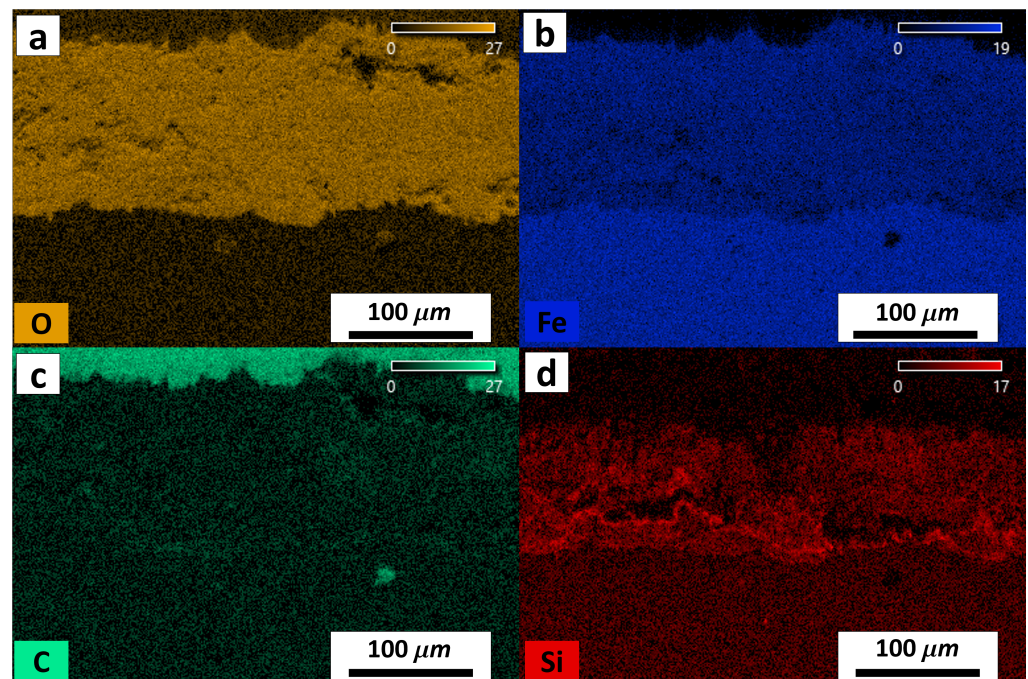


**Figure 4.** EDS mapping of SiMo nodular iron: (a) Oxygen concentration map. (b) Fe concentration map. (c) C concentration map. (d) Si concentration map.

Previously, Ekström et al. [16] indicated that SiMo has a multilayered oxide scale consisting of outer layers of Fe-rich oxide phases ( $\text{Fe}_2\text{O}_3$  or  $\text{Fe}_3\text{O}_4$ ), an underlying subscale composed of a mixture of Fe-rich and Fe-Si rich oxide, and a discontinuous barrier layer of silica at the oxide/metal interface at  $700\text{ }^\circ\text{C}$ – $800\text{ }^\circ\text{C}$ . Carbides and nodules of both

oxidized and unoxidized graphite were found in the sublayer, as well as a duplex layer of oxide structure and oxide phases. Although the current study reproduced most of these findings (oxidized graphite, duplex layer of oxide structure, and oxide phases), it did not detect any unoxidized graphite nodules within the scale. In addition, previous research suggested [24] that the silica layer transformed into fayalite and iron oxide at 800 °C. This change happened through a series of events. Ebel et al. further explained that during this transformation, austenite grains formed at the boundary between the matrix and silica, which induced stress and led to fractures in the silica layer. Consequently, the iron oxide can expand, which displaces the original silica particles. Similar results were discussed by Lakekh et al. [27] from the decarburization point of view. It was claimed that the continuous and protective silica layer was restricted at 700 °C since the oxygen permeability of silica increased at 750 °C and induced the decarburization reaction near the interface. The metal matrix deformed under the high pressure of CO gas produced during decarburization. As a result, the brittle silica layer delaminated. Considering all of these factors, it is more probable that fayalite ( $\text{Fe}_2\text{SiO}_4$ ) formed at the metal/oxide interface in the current study. As a result, silicon is the main contributor to the oxidation resistance of SiMo nodular cast iron.

**Table 2.** EDS point analysis of SiMo nodular iron in atomic %.

Atomic %	O	Fe	Si	Mo	C
P1	55.3	28.3	8.2	0.0	8.3
P2	55.0	38.1	0.3	0.0	6.6
P3	50.8	25.5	8.7	0.0	14.9
P4	0.0	80.5	6.4	0.0	13.1

After the oxidation characteristics of SiMo nodular cast iron were described, the influence of aluminum on the isothermal oxidation behavior was discussed. Further analysis of oxide morphology for SiMoAl cast irons (SiMo3Al and SiMo4Al) exhibited different behavior and demonstrated enhanced resistance to oxidation. Figure 5 displays the oxidation scale that grew on the SiMoAl-cast iron over a duration of 96 h at a temperature of 800 °C. The oxide layer seen was thin and dense with respect to SiMo.

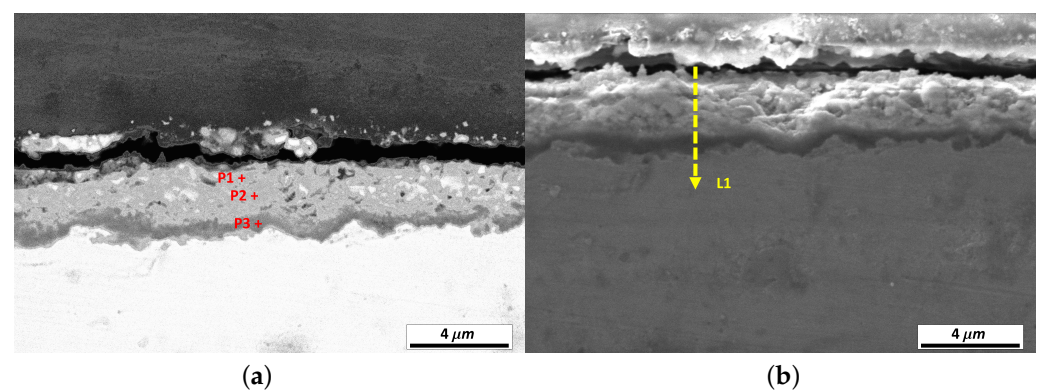


**Figure 5.** Cross-sectional SEM images of oxide layer of (a) SiMo3Al; and (b) SiMo4Al. P1, P2, and P3 are the EDS points, and the yellow line L1 shows the line scan direction.

Two key findings should be emphasized from the SEM/EDS analysis (Figures 5 and 6, and Table 3): one is the formation of an Al-rich oxide layer, and the other is the nature of the decarburized graphite pits. Similar to SiMo nodular iron, a multilayer oxide film was observed (Figure 5), but the oxide morphology and phases were different than the SiMo iron. The external solid oxide film of the SiMo3Al sample consisted of iron-rich oxides, while an aluminum-rich oxide phase at the interface could be seen forming a continuous thin oxide layer. Aluminum has a higher affinity to oxygen than to iron and silicon. It

was known that aluminum oxide ( $\text{Al}_2\text{O}_3$ ) has high thermodynamic stability at  $800^\circ\text{C}$  as compared to  $\text{Fe}_2\text{O}_3$ ,  $\text{SiO}_2$ , and  $\text{Fe}_2\text{SiO}_4$  [29]. Thus, a dense and compact alumina layer formed at the interface, which acted as a protective barrier by impeding the diffusion of oxygen. In contrast to the SiMo nodular iron, Si-rich oxide phases were not observed since  $\text{Al}_2\text{O}_3$  is more stable thermodynamically than  $\text{SiO}_2$ . These aluminum-rich oxide structures are favorable for parts exposed to high temperatures.

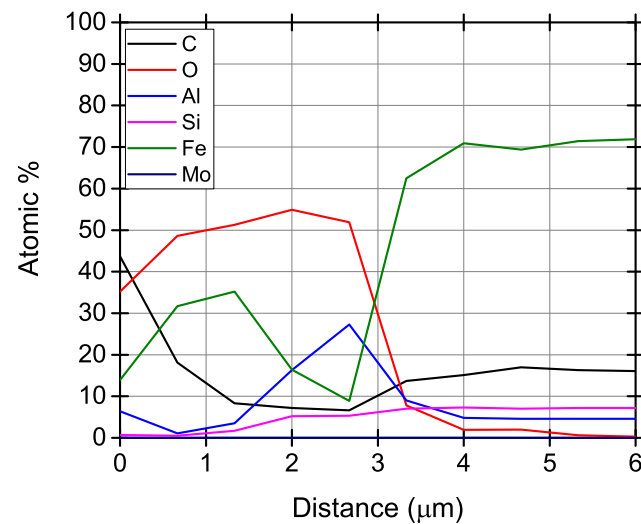


**Figure 6.** EDS line scan of SiMo4Al sample.

**Table 3.** EDS point analysis of SiMo3Al in atomic%.

Atomic %	O	Fe	Al	Si	Mo	C
P1	52.4	36.0	1.2	0.6	0.0	9.8
P2	51.7	34.0	1.3	1.0	0.0	12.0
P3	53.9	9.5	25.9	4.1	0.0	6.6

SiMo4Al showed similar oxide morphologies and phases to SiMo3Al. As the aluminum content of the matrix increased, the thickness of the oxide film, particularly the iron-rich external oxide layer, decreased. In the top section, the concentration of iron was relatively higher compared to the concentrations of aluminum and silicon. However, a thin, continuous alumina film formed at the interface that reduced oxygen diffusion to the matrix. EDS line scans are displayed in Figure 6. Through the metal matrix, the concentration of silicon and iron increased, while the amount of aluminum and oxygen decreased. Furthermore, it was shown in the previous section that when the amount of aluminum was increased from 3.5 wt% to 4.8 wt%, coarse  $\kappa$  carbide structures were formed. The presence of the  $\kappa$ -carbide phase was not detrimental to the oxidation resistance of SiMo4Al, as compared to the oxide film thicknesses. The mass fraction of the  $\kappa$  carbide phase, as determined in Figure 1, indicated that this complex carbide phase was not stable around  $800^\circ\text{C}$  and dissolved into the ferrite matrix.

These findings are in agreement with previous studies. Lakeh et al. [27,39] studied the oxidation behavior of SiMo alloying with 3.0 wt% Si, 1.8 wt% Al, and 3 wt% Al at  $800^\circ\text{C}$  for 100 h. Like the present study, multilayer oxide scale was observed. The external scale was composed of iron-rich oxides, while the internal scale consisted of aluminum- and iron-rich oxides, and the thin alumina layer with a thickness of 50 nm was observed at the interface between oxide and metal. It was indicated that the microstructure was fully ferritic with mostly spheroidal graphite. Unlike in the current study, it was indicated that microstructure exhibited complete ferritic characteristics and predominantly consisted of spherical graphite due to the relatively low concentration of silicon, aluminum, and carbon in comparison to the present study.

Comparative film thicknesses of SiMo and SiMoAl are given in Figure 7. It was obvious to see that the thickness of the oxide layer was significantly decreased by the addition of Al into SiMo. The oxide film thickness of SiMo was 144.4 microns, while SiMo4Al had an oxide thickness of only 2.9 microns. Nevertheless, there were no substantial disparities in thickness between SiMo3Al and SiMo4Al. It is believed that the oxidation resistance is saturated and that the addition of aluminum above 4.8% does not significantly alter the oxidation resistance. In the literature, Ebel et al. [24] demonstrated that an oxide scale 130 micron thick was formed after 100 h of heating at 800 °C for SiMo nodular iron. Lakeh et al. reported that thickness of the scale formed in SiMo with 3.5 wt% Si and 3 wt% Al cast iron was 5 to 15 microns at the test temperatures of 650 °C and 800 °C.

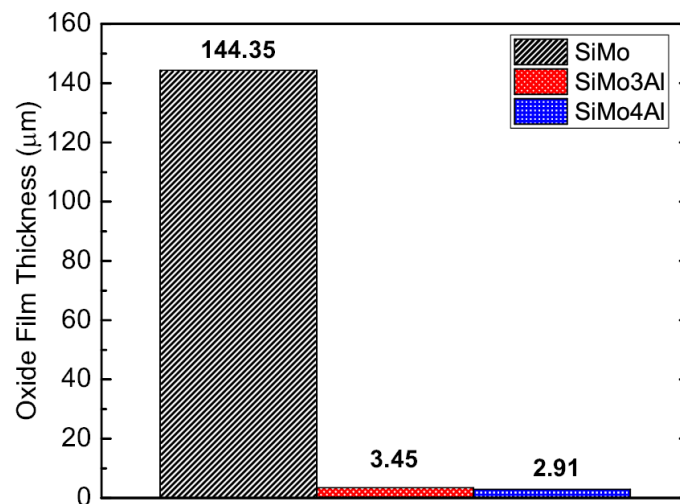


**Figure 7.** Average oxide film thickness of SiMo and SiMoAl samples.

Regarding cast iron oxidation, the other important finding was the nature of the decarburized graphite pits. Graphite is unstable at temperatures above 600 °C and oxidizes quickly in air. Thus, graphite–iron boundaries provide efficient channels for the transport of oxygen through the material, causing subsurface oxidation. However, the morphology and the distribution of graphite were regarded as determining factors in the high-temperature oxidation resistance of cast irons. Flake and vermicular graphite cast iron are reported to exhibit worse high-temperature oxidation resistance than the spheroidal graphite cast iron [29,30]. Flake and vermicular graphite were almost interconnected, while spheroidal graphite itself was present in the matrix in the form of separate agglomerates. Due to the oxidation of graphite, subsurface oxidation was observed in Figure 8. These decarburized pits were predominantly covered by aluminum oxide. Iron oxides were not observed. Due to the low oxidation activation energy of graphite with respect to the metal matrix, oxidation started with the graphite precipitates and continued with exposed alloying elements. In this circumstance, after decarburization, segregated aluminum surrounding the graphite precipitates was directly exposed to the oxidizing air environment and quickly formed alumina scale without the formation of hematite. This is in contrast to findings by Rashid et al. [46], who demonstrated that even when close to the surface, the decarburization of nodular graphite was prevented by 6.6 wt% Al or more at 550 °C. Similar findings to Rashid et al. were also suggested by Lakeh et al. [27,39] that the addition of aluminum decreased the decarburization layer thickness of nodular graphite since the decarburization of nodular graphite occurred due to the oxygen transport along the grain boundaries. The current study suggests that in contrast to previous studies, subsurface oxidation was not eliminated or decreased by the decarburization rate due to the interconnected morphology of graphite. This can potentially be explained by the fact that decarburized graphite pits covered by aluminum oxides were linked to the surface graphite.

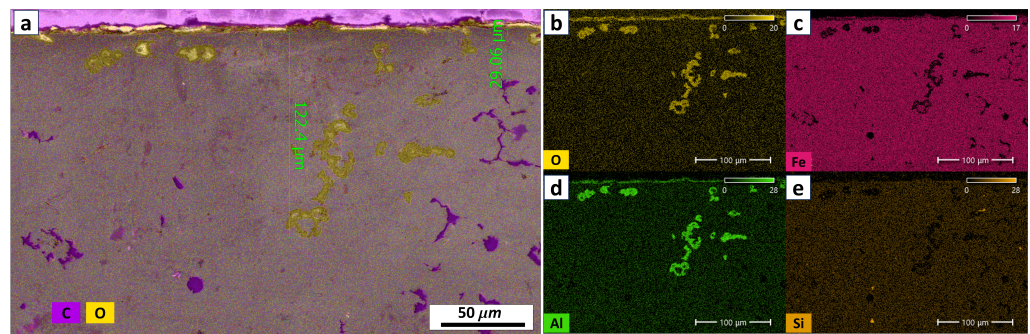


**Figure 8.** SEM/EDS mapping of SiMo4Al sample. (a) Decarburization depth on the surface of SiMo4Al. Oxidized and unoxidized graphites are displayed by yellow and purple, respectively. (b) Oxygen concentration map. (c) Iron concentration map. (d) Aluminum concentration map. (e) Silicon concentration map.

Overall, considering the isothermal oxidation test results, the SiMo4Al sample showed better static oxidation resistance than the literature [27,39], although it contained vermicular graphite and coarse  $\kappa$  carbides in the microstructure.

### 3.3. Nonisothermal Oxidation Mechanism of SiMo and SiMoAl

Figure 9a–d shows a comparison of the TG and DTG curves of SiMo and SiMoAl cast irons and graphite for a range of heating rates. As a point of comparison, highly purified graphite was utilized. The exothermic reaction can be divided into two distinct reactions that occur simultaneously: the oxidation process of metals and the decarburization or oxidation of graphite precipitates. The measured TG signal revealed the overall change in weight as a result. TG curves seen in Figure 9a–c can be described in two stages: Stage 1 took place at a temperature between RT and 700 °C. The weight gain rate was quite low in this region. The second stage, which had a higher weight loss rate, took place at temperatures above 700 °C. At this stage, the decarburization reaction rate was greater than the oxidation reaction rate for each composition.

The effective oxidation activation energy of each composition was calculated from thermogravimetric analysis by using the Kissinger method. According to these calculations, the predicted energies of SiMo, SiMo3Al, and SiMo4Al were 152, 223.5, and 233.7 kJ/mol, respectively. Additionally, the decarburization of high-purity hot isostatic-pressed graphite resulted in an activation energy of 123 kJ/mole. Previously, Ebel et al. [24] calculated the oxidation activation energy of SiMo nodular iron at 158 kJ/mol by using the oxide film thicknesses as a function of thermal cycles. Results from the current study are in alignment with these previously reported values.

As shown in Figure 10, the presence of aluminum increased the effective activation energy of oxidation. However, comparing the aluminum-containing samples revealed that their activation energies were very close to each other. Aluminum oxides exhibited greater thermodynamic stability in comparison to iron oxides and silicon oxides. Therefore, the addition of aluminum led to the formation of aluminum-rich oxides on the surface whose oxygen permeability was significantly less than that of iron oxides [47]. This layer acted as an oxygen diffusion barrier and increased the effective activation energy of oxidation.

When the outcomes of the isothermal oxidation test were combined with the ones shown here, a clear and consistent correlation between the thickness of the oxide scales and the activation energies of oxidation was observed. Furthermore, the activation energies of Al-alloyed samples exhibited minor variation, indicating that the oxidation resistance was getting closer to the threshold.

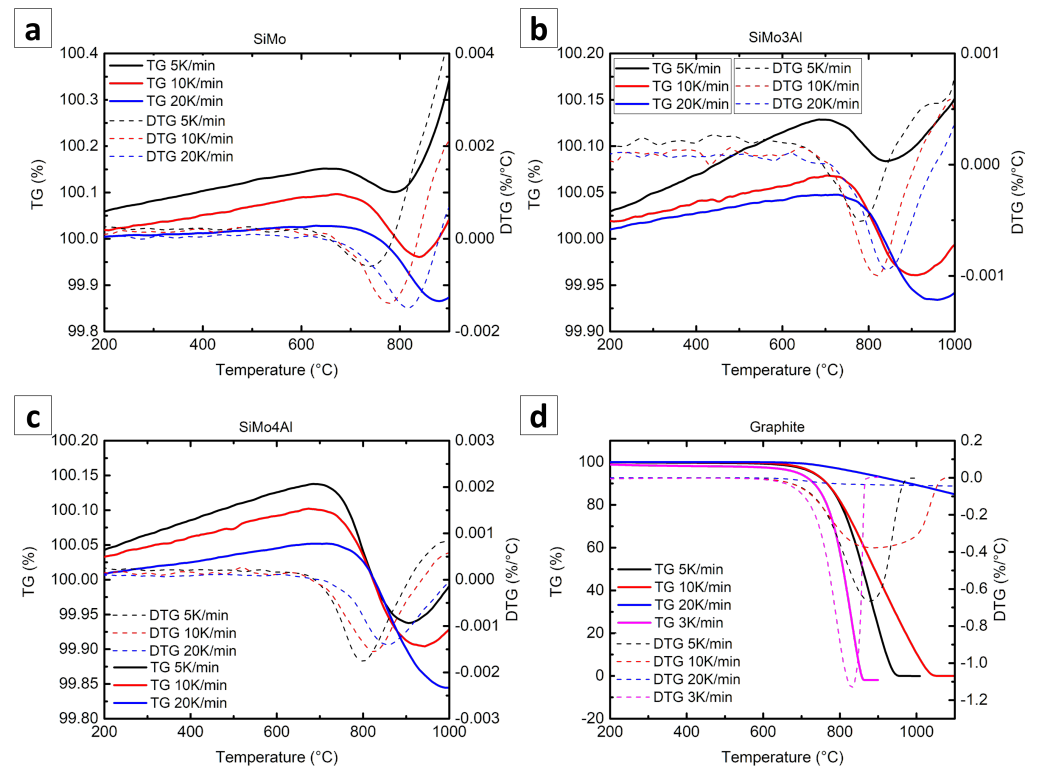


Figure 9. TG and DTG curves: (a) SiMo. (b) SiMo3Al. (c) SiMo4Al. (d) Graphite.

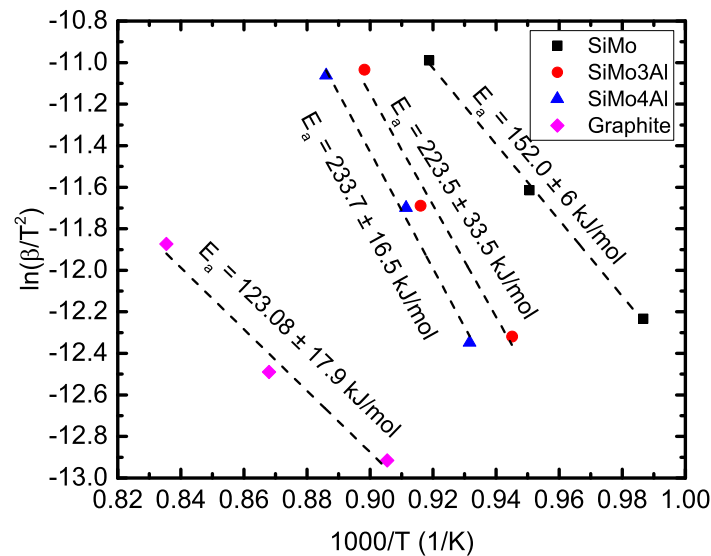
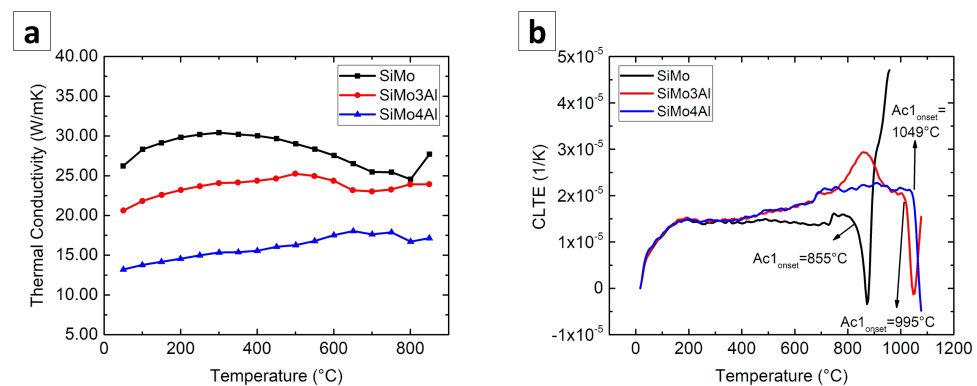


Figure 10. Effective activation energy of oxidation.

### 3.4. Thermophysical Properties of SiMoAl

In addition to the high-temperature oxidation behavior of SiMoAl vermicular graphite cast iron, thermophysical properties were also essential for high-temperature applications. The thermal conductivity and thermal expansion coefficient are investigated and compared with the reference material of SiMo in Figure 11. As seen in Figure 11a, the thermal conductivity of the material decreased with respect to the amount of aluminum that is contained in the cast iron structure.



**Figure 11.** Comparison of (a) thermal conductivity and (b) thermal expansion coefficient.

The studies [48,49] on the effects of alloying elements on ferrite and graphite cast irons showed that almost all of the elements cause a decrease in thermal conductivity. Notably, aluminum and silicon affected cast iron's thermal conductivity more than other elements. Alloying elements not only dissolve in the ferrite matrix but also exert a substantial influence on the microstructure, as detailed in Section 3.1. It was clearly seen that the existence of the  $\kappa$  carbide phase led to a substantial decrease in thermal conductivity.

A comparison within the SiMoAl samples revealed that SiMo4Al exhibited lower thermal conductivity. This reduction was attributed to the formation of  $\kappa$  carbide, which has a low thermal conductivity of its own. It was also considered that the formation of  $\kappa$  carbide decreased the mass fraction of graphite and the ferrite (bcc) phase in the structure. As temperatures increased, the amount of the  $\kappa$  phase decreased, with the aluminum in the  $\kappa$  phase dissolving into the iron matrix. Consequently, this dissolution resulted in no discernible alteration in thermal conductivity measurements, as illustrated in Figure 11. The CALPHAD approach was employed to calculate normalized mass fractions for the Fe-Al-Si-C system, as shown in Figure 12, utilizing literature data for defining thermodynamic and crystallographic parameters [50–53].

Additionally, graphite morphology emerged as a significant factor influencing thermal conductivity [54]. Lamellar graphite iron and vermicular graphite iron exhibited higher thermal conductivity than nodular graphite iron due to their extensive three-dimensional interconnected graphite networks. In contrast, nodular iron had a larger mean free path of the matrix that linked the graphite nodules [55], and this reduced the transfer of heat through the matrix. However, the presence of aluminum in the matrix made SiMoAl samples less thermally conductive, even if they had a vermicular graphite structure. In essence, the alloying effect of aluminum exerted a more substantial influence on thermal conductivity than the effect of graphite morphology.

The other critical thermophysical property is the thermal expansion coefficient discussed in this study. According to the dilatometric measurements, the SiMoAl samples exhibited nearly identical thermal expansions but had higher thermal expansion coefficients than the reference material of SiMo. It was observed that there was a slight increase above 400 °C in the thermal expansion coefficient of SiMoAl cast irons. However, it was considered that the expansion coefficient remained at reasonable values for hot-end exhaust components.

Another important result to be reached from the dilatometer measurement was the determination of ferrite–austenite phase-transition (Ac1) temperatures. It was clearly seen that the Ac1 temperature shifted to higher temperatures with the addition of aluminum. These measured Ac1 temperatures were also used in the thermodynamic model validation for calculating the normalized mass fractions of the phases mentioned above. The correlation between the thermodynamic model and the experiment was acceptable.

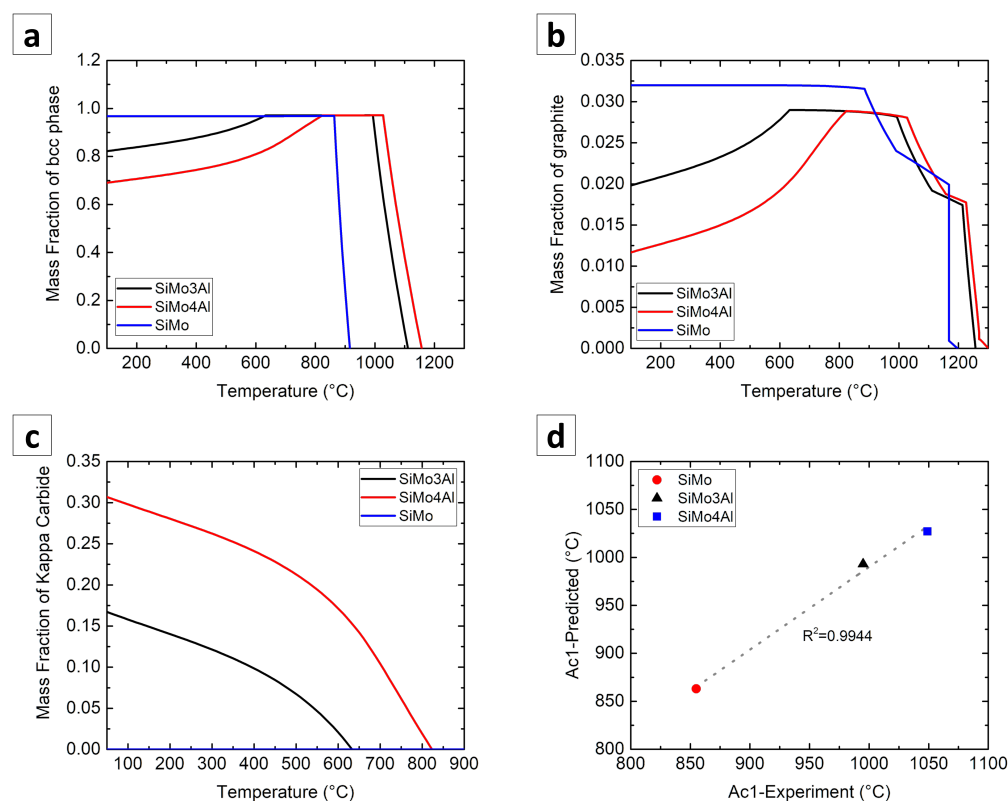


**Figure 12.** (a) Normalized mass fraction of bcc (ferrite) phase. (b) Normalized mass fraction of graphite. (c) Normalized mass fraction of  $\kappa$  carbide phase. (d) Correlation plot of Ac1 temperatures.

#### 4. Conclusions

The impact of high-Al alloying on the microstructure, thermophysical properties, and high-temperature oxidation behavior of high SiMoAl vermicular graphite cast iron was investigated from several perspectives. The following conclusions were reached:

- The addition of aluminum (above 3.0 wt%) combined with 4.2 wt% Si induced an increase in the amount of pearlitic two-phase lamellar structure and coarse-grained  $\kappa$  carbide, although ferrite predominated in SiMo nodular iron.
- A dense and compact alumina layer formed at the interface, which acted as a protective barrier by impeding the diffusion of oxygen.
- The thickness of the oxide layer was significantly reduced with the addition of aluminum.
- Severe subsurface oxidation was seen due to the interconnected vermicular graphite, but this was covered by aluminum oxides after decarburization. Iron oxides were not observed at the subsurface.
- While the oxidation characteristics of vermicular graphite cast iron were inferior to those of ductile graphite cast iron, the addition of aluminum enhanced SiMoAl iron's high-temperature oxidation resistance and longevity.
- The effective oxidation activation energy of SiMo nodular and SiMoAl vermicular graphite cast iron was estimated from nonisothermal thermogravimetric analysis by Kissinger method.
- The effective activation energy of oxidation was increased by the addition of aluminum; nonetheless, the activation energies of Al alloy samples showed slight differences among themselves, suggesting that the oxidation resistance was approaching the threshold.
- Thermal conductivity dramatically decreased with the addition of aluminum. The mass fraction of  $\kappa$  carbide, graphite morphology, and aluminum solubility in ferrite have significant roles.

- SiMoAl vermicular graphite cast irons (SiMo3Al, SiMo4Al) were found to have higher thermal expansion, especially above 400 °C, but when SiMo3Al and SiMo4Al were compared among themselves, it was seen that the amount of aluminum had no effect on thermal expansion.
- The addition of aluminum led to increased Ac1 temperatures. This provides a broad operating temperature range for high-temperature applications.

In addition to these, potentially as a result of  $\kappa$  carbide precipitate hardening, SiMoAl cast irons are considered to have elevated thermomechanical properties. These characteristics make SiMoAl cast irons a promising candidate for hot-end exhaust components.

**Author Contributions:** Conceptualization, R.Y., F.B. and N.S.; methodology, R.Y. and N.S.; investigation, R.Y.; data analysis, R.Y.; data curation, R.Y.; writing—original draft preparation, R.Y.; writing—review and editing, F.B. and N.S.; supervision, N.S.; funding acquisition, N.S. All authors have read and agreed to the published version of the manuscript.

**Funding:** This research received no external funding.

**Data Availability Statement:** The data presented in this study are available on request from the corresponding author. The data are not publicly available due to privacy.

**Acknowledgments:** The authors would like to thank Cem Kincal from Istanbul Technical University for their support on thermal characterization.

**Conflicts of Interest:** Author Rifat Yilmaz was employed by the company Ford Otomotiv Sanayi A.S., Sancaktepe R & D Center. The remaining authors declare that the research was conducted in the absence of any commercial or financial relationships that could be construed as a potential conflict of interest.

## Abbreviations

The following abbreviations are used in this manuscript:

DSC	Differential scanning calorimetry
DTG	Derivative thermogravimetry
EDS	Energy-dispersive X-ray spectroscopy
SEM	Scanning electron microscope
LFA	Laser flash analysis
TG	Thermogravimetry
XRD	X-ray diffraction analysis
CALPHAD	Computer coupling of phase diagrams and thermochemistry

## References

1. Li, Y.; Liu, J.; Huang, W.; Wu, Y. Failure Analysis of a Diesel Engine Exhaust Manifold. *Int. J. Met.* **2023**, *17*, 538–550. [[CrossRef](#)]
2. Kihlberg, E.; Norman, V.; Skoglund, P.; Schmidt, P.; Moverare, J. On the correlation between microstructural parameters and the thermo-mechanical fatigue performance of cast iron. *Int. J. Fatigue* **2021**, *145*, 106112. [[CrossRef](#)]
3. Ekstrom, M.; Jonsson, S. High-temperature mechanical and fatigue properties of cast alloys intended for use in exhaust manifolds. *Mater. Sci. Eng. A* **2014**, *616*, 78–87. [[CrossRef](#)]
4. Xiang, S.; Jonsson, S.; Hedstrom, P.; Zhu, B.; Odqvist, J. Influence of ferritic nitrocarburizing on the high-temperature corrosion-fatigue properties of the Si-Mo-Al cast iron SiMo1000. *Int. J. Fatigue* **2021**, *143*, 105984. [[CrossRef](#)]
5. Pierce, D.; Haynes, A.; Hughes, J.; Graves, R.; Maziasz, P.; Muralidharan, G.; Shyam, A.; Wang, B.; England, R.; Daniel, C. High temperature materials for heavy duty diesel engines: Historical and future trends. *Prog. Mater. Sci.* **2019**, *103*, 109–179. [[CrossRef](#)]
6. Xiang, S.; Hedström, P.; Zhu, B.; Linder, J.; Odqvist, J. Influence of graphite morphology on the corrosion-fatigue properties of the ferritic Si-Mo-Al cast iron SiMo1000. *Int. J. Fatigue* **2020**, *140*, 105781. [[CrossRef](#)]
7. Bartosak, M.; Horvath, J. Isothermal low-cycle fatigue, fatigue-creep and thermo-mechanical fatigue of SiMo 4.06 cast iron: Damage mechanisms and life prediction. *Eng. Fract. Mech.* **2023**, *228*, 109316. [[CrossRef](#)]
8. Quan, G.; Li, D.; Wu, X. *Thermo-Mechanical Fatigue (TMF) Life of Ductile SiMo Cast Iron with Aluminum Addition*; SAE Technical Paper 2021-01-0281; SAE International: Warrendale, PA, USA, 2021.
9. Oberg, C.; Zhu, B.; Jonsson, S. Creep behaviour, creep damage and precipitation in the austenitic ductile cast iron D5S at 750 °C. *Mater. Sci. Eng. A* **2021**, *802*, 140662. [[CrossRef](#)]

10. Joshi, A.; Baxevanakis, K.P.; Silberschmidt, V.V. High-Temperature Creep of Cast Irons. In *Solid Mechanics, Theory of Elasticity and Creep. Advanced Structured Materials*; Altenbach, H., Mkhitarjan, S.M., Hakobyan, V., Sahakyan, A.V., Eds.; Springer: Cham, Switzerland, 2023; p. 159.
11. Franzen, D.; Pustal, B.; Buhrig-Polaczek, A. Mechanical Properties and Impact Toughness of Molybdenum Alloyed Ductile Iron. *Int. J. Met.* **2021**, *15*, 983–994. [[CrossRef](#)]
12. Guzik, E.; Kopycinski, D.; Wierzychowski, D. Manufacturing of Ferritic Low-Silicon and Molybdenum Ductile Cast Iron with the Innovative 2PE-9 Technique. *Arch. Metall. Mater.* **2014**, *59*, 687–691. [[CrossRef](#)]
13. Chavan, S.; Khandelwal, H. Effect of Mo on Micro-structural and Mechanical Properties of As-Cast Ferritic Spheroidal Graphite Iron. *Trans. Indian Inst. Met.* **2021**, *74*, 2703–2711. [[CrossRef](#)]
14. Zhu, W.; Pint, B.A.; Huo, Y.; Godlewski, L.; Ghaffari, B.; Lekakh, S.; Engler-Pinto, C.; Li, M. The Oxidation of the HiSiMo Cast Irons Alloyed with Cr/Al at 800 °C. *Oxid. Met.* **2022**, *97*, 441–449. [[CrossRef](#)]
15. Tholence, F.; Norell, M. High Temperature Corrosion of Cast Alloys in Exhaust Environments I-Ductile Cast Irons. *Oxid. Met.* **2008**, *69*, 13–36. [[CrossRef](#)]
16. Ekstrom, M.; Szakalos, P.; Jonsson, S. Influence of Cr and Ni on High-Temperature Corrosion Behavior of Ferritic Ductile Cast Iron in Air and Exhaust Gases. *Oxid. Met.* **2013**, *80*, 455–466. [[CrossRef](#)]
17. Ebel, A.; Brou, S.Y.; Malard, B.; Lacaze, J.; Monceau, D.; Vaissière, L. High-Temperature Oxidation of a High Silicon SiMo Spheroidal Cast Iron in Air with In Situ Change in H<sub>2</sub>O Content. *Mater. Sci. Forum* **2018**, *925*, 353–360. [[CrossRef](#)]
18. Brady, M.P.; Muralidharan, G.; Leonard, D.N.; Haynes, J.A.; Weldon, R.G.; England, R.D. Long-Term Oxidation of Candidate Cast Iron and Stainless Steel Exhaust System Alloys from 650 to 800 °C in Air with Water Vapor. *Oxid. Met.* **2014**, *82*, 359–381. [[CrossRef](#)]
19. Lekakh, S.N.; Bofah, A.; Godlewski, L.A.; Li, M. Effect of Micro-Structural Dispersity of SiMo Ductile Iron on High Temperature Performance during Static Oxidation. *Metals* **2022**, *12*, 661. [[CrossRef](#)]
20. Lekakh, S.N.; Bofah, A.; Osei, R.; O'malley, R.; Godlewski, L.; Li, M. High Temperature Oxidation and Decarburization of SiMo Cast Iron in Air and Combustion Atmospheres. *Oxid. Met.* **2021**, *95*, 251–268. [[CrossRef](#)]
21. Khalvan, M.M.; Divandari, M. High-Temperature Oxidation Behavior of Spheroidal Graphite Cast Irons Containing up to 7.5 wt% Aluminum at 750 °C in Static Air. *Oxid. Met.* **2022**, *98*, 65–75. [[CrossRef](#)]
22. Reynaud, A. Corrosion of Cast Irons. In *Shreir's Corrosion*; Cottis, B., Graham, M., Lindsay, R., Lyon, S., Richardson, T., Scantlebury, D., Stott, H., Eds.; Elsevier: Amsterdam, The Netherlands, 2010; p. 1741.
23. Logani, R.C.; Smeltzer, W.W. The development of the wustite-fayalite scale on an iron-1.5 wt.% silicon alloy at 1000 °C. *Oxid. Met.* **1971**, *3*, 15–32. [[CrossRef](#)]
24. Ebel, A.; Marsan, O.; Lacaze, J.; Malard, B. Cyclic oxidation of high-silicon spheroidal graphite iron. *Corros. Sci.* **2021**, *192*, 109854. [[CrossRef](#)]
25. Svedung, I.; Vannerberg, N.G. The influence of silicon on the oxidation properties of iron. *Corros. Sci.* **1974**, *14*, 391–399. [[CrossRef](#)]
26. Liu, L.L.; Guo, Q.Q.; Niu, Y. Transition between different oxidation modes of binary Fe–Si alloys at 600–800 °C in pure O<sub>2</sub>. *Oxid. Met.* **2013**, *79*, 201–224. [[CrossRef](#)]
27. Lekakh, S.N.; Bofah, A.; Chen, W.-T.; Godlewski, L.; Li, M. Prevention of high-temperature surface degradation in SiMo Cast Irons by Cr and Al alloying. *Metall. Mater. Trans. B* **2020**, *51*, 2542–2554. [[CrossRef](#)]
28. Yamaguchi, Y.; Kiguchi, S.; Sumimoto, H.; Nakamura, K. Effect of graphite morphology on decarburized cast iron. *Int. J. Cast Met. Res.* **2003**, *16*, 137–142. [[CrossRef](#)]
29. Lin, M.B.; Wang, C.J.; Volinsky, A.A. High Temperature Oxidation Behavior of Flake and Spheroidal Graphite Cast Irons. *Oxid. Met.* **2011**, *76*, 161–168. [[CrossRef](#)]
30. Guo, Q.; Yang, Z.; Guo, D.; Tao, D.; Guo, Y.; Li, J.; Bai, Y. Research on the Oxidation Mechanism of Vermicular Graphite Cast Iron. *Materials* **2019**, *12*, 3130. [[CrossRef](#)] [[PubMed](#)]
31. Ibrahim, M.M.; Nofal, A.; Mourad, M.M. Microstructure and Hot Oxidation Resistance of SiMo Ductile Cast Irons Containing Si-Mo-Al. *Metall. Mater. Trans. B* **2017**, *48*, 1149–1157. [[CrossRef](#)]
32. Kleiner, S.; Track, K. Simo1000 ein aluminiumlegiertes gusseisen für hochtemperaturanwendungen. *Giesserei* **2010**, *97*, 28–34.
33. Aktaş Çelik, G.; Atapek, Ş.H.; Polat, Ş.; Tzini, M.I.T.; Haidemenopoulos, G.N. Hot Oxidation Resistance of a Novel Cast Iron Modified by Nb and Al Addition for Exhaust Manifold Applications. *Metall. Mater. Trans. A* **2022**, *53*, 1991–2003. [[CrossRef](#)]
34. Aktaş Çelik, G.; Atapek, Ş.H.; Polat, Ş. Initial Oxidation Stage of SiMo and SiNb-xAl Ductile Cast Irons in Air and CO<sub>2</sub>-Containing Atmospheres. *Int. J. Met.* **2023**, *17*, 1763–1777. [[CrossRef](#)]
35. Cvetnic, C.R.; Ravindran, C.; McLean, A. A Study of Oxidation of Ductile Iron Alloyed with Molybdenum, Silicon and Aluminum. *Can. Metall. Q.* **2007**, *46*, 75–88. [[CrossRef](#)]
36. Reynaud, A.; Roberge, J.L. Application of high temperature spheroidal graphite cast irons in exhaust manifolds. *Fonderie Fonduer d'Aujourd'hui* **1999**, *182*, 37–41.
37. Yaker, J.A.; Byrnes, L.E.; Leslie, W.C.; Petitbon, E.U. Microstructures and Strength of Aluminum-Containing Gray and Nodular Irons in the Temperature Range 1200–1800 F (649–982 C). *AFS Trans.* **1976**, *84*, 305–320.
38. Petitbon, E.U.; Wallace, J.F. Aluminum Alloyed Gray Iron Properties at Room and Elevated Temperature. *AFS Cast Met. Res. J.* **1973**, *9*, 127–134.

39. Lekakh, S.N.; Johnson, C.; Godlewski, L.; Li, M. Control of High-Temperature Static and Transient Thermomechanical Behavior of SiMo Ductile Iron by Al Alloying. *Int. J. Met.* **2023**, *17*, 22–38. [[CrossRef](#)]
40. Kissinger, H.E. Variation of peak temperature with heating rate in differential thermal analysis. *J. Res. Natl. Bur. Stand.* **1956**, *57*, 217–221. [[CrossRef](#)]
41. Kissinger, H.E. Reaction kinetics in differential thermal analysis. *Anal. Chem.* **1957**, *29*, 1702–1706. [[CrossRef](#)]
42. Mampaey, F. Aluminium Cast Iron. *AFS Trans.* **2005**, *113*, 105–149.
43. Boeri, R.; Weinberg, E. Microsegregation in ductile iron. *AFS Trans.* **1989**, *97*, 179–184.
44. Datta, N.K.; Engel, N.N. Electron microprobe study of the distribution of Si, Cu, Ni, Mn, Mo, and Cr in ductile iron. *AFS Trans.* **1976**, *84*, 431–436.
45. Liu, P.C.; Loper, C.R. Segregation of certain elements in cast irons. *AFS Trans.* **1984**, *92*, 289–295.
46. Kiani Rashid, A.R.; Edmonds, D.V. Oxidation behavior of Al-alloyed ductile cast irons at elevated temperature. *Surf. Interface Anal.* **2004**, *36*, 1011–1013. [[CrossRef](#)]
47. Barin, I. *Thermochemical Data of Pure Substances*, 3rd ed.; VCH: Weinheim, Germany; New York, NY, USA, 2008.
48. Wang, G.; Li, Y. Thermal conductivity of cast iron—A review. *China Foundry* **2020**, *17*, 85–95. [[CrossRef](#)]
49. Wang, G.; Li, Y. Effects of alloying elements and temperature on thermal conductivity of ferrite. *J. Appl. Phys.* **2019**, *126*, 125118. [[CrossRef](#)]
50. Zheng, W.; He, S.; Selleby, M.; He, Y.; Li, L.; Lu, X.G.; Ågren, J. Thermodynamic assessment of the Al-C-Fe system. *Calphad* **2017**, *58*, 34–49. [[CrossRef](#)]
51. Grobner, J.; He, S.; Lukas, H.L.; Aldinger, F. Thermodynamic calculation of the ternary system Al-Si-C. *Calphad* **1996**, *20*, 247–254. [[CrossRef](#)]
52. Liu, Z.K.; Chang, Y.A. Thermodynamic assessment of the Al-Fe-Si system. *Metall. Mater. Trans. A* **1999**, *30*, 1081–1095. [[CrossRef](#)]
53. Lacaze, J.; Sundman, B. An assessment of the Fe-C-Si system. *Metall. Mater. Trans. A* **1991**, *21*, 2211–2223. [[CrossRef](#)]
54. Jiang, A.; Shao, A.; Song, L.; Hua, M.; Zheng, H.; Zhang, X.; Tian, X.; Lin, X. A New Theoretical Method for Studying Effects of Microstructure on Effective Thermal Conductivity of Vermicular Graphite Cast Iron. *Materials* **2023**, *16*, 2158. [[CrossRef](#)]
55. Blackmore, P.A.; Morton, K. Structure-property relationships in graphitic cast irons. *Int. J. Fatigue* **1982**, *4*, 149–155. [[CrossRef](#)]

**Disclaimer/Publisher’s Note:** The statements, opinions and data contained in all publications are solely those of the individual author(s) and contributor(s) and not of MDPI and/or the editor(s). MDPI and/or the editor(s) disclaim responsibility for any injury to people or property resulting from any ideas, methods, instructions or products referred to in the content.